ASME Journal of Electronic Packaging
Online journal at:
https://asmedigitalcollection.asme.org/electronicpackaging

# Computational Fluid Dynamics Modeling and Optimization of Large-Scale (3 CM × 3 CM) Silicon-Based Embedded Microchannels With Three-Dimensional Manifold Microcoolers

**Daeyoung Kong**
Department of Mechanical Engineering,
Stanford University,
Stanford, CA 94305

**Heungdong Kwon**
Department of Mechanical Engineering,
Stanford University,
Stanford, CA 94305

**Haeun Lee**
Department of Mechanical Engineering,
Chung-Ang University,
Seoul 06974, South Korea

**Hyoungsoon Lee**
Department of Mechanical Engineering,
Chung-Ang University,
Seoul 06974, South Korea

**Mehdi Asheghi**
Department of Mechanical Engineering,
Stanford University,
Stanford, CA 94305

**Kenneth E. Goodson**[1]
Department of Mechanical Engineering,
Stanford University,
Stanford, CA 94305

*The continuing increase in central processing unit and graphic processing unit performances can be attributed mostly to the rise in frequency, scaling of chip area (bigger dies), advancements in thermal management, and improvements in thermal design power, among other factors. Over the past two decades, the size of a typical graphic processing unit die has increased from 100 mm$^2$ to ∼800 mm$^2$ in the year 2020. Silicon-based single-phase embedded microchannels with a large area of 30 mm × 30 mm, featuring three-dimensional (3D) manifold (MF) μ-coolers, can potentially remove heat and minimize pressure drop. However, previous computational fluid dynamics simulation findings indicated considerable temperature nonuniformity resulting in increased thermal resistance and maximum temperature. The primary cause of temperature nonuniformity is the abrupt flow acceleration at the entrance and sudden deceleration at the end section of the 3D-manifold inlet channels. This leads to a significant temperature rise in the middle region of the microcooler. In this study, we introduce innovative microcooler designs and conduct extensive computational fluid dynamics simulation to achieve low thermal resistance, low-pressure drop, and crucially, uniform temperature distribution across the entire surface area of the microprocessor. To deal with this issue, our initial approach involved integrating converging inlet and diverging outlet channels into the 3D manifold. Although this method effectively dealt with nonuniformity throughout the μ-cooler's area, it still resulted in a large pressure drop. Consequently, we implemented a narrow opening at the end of the inlet channels in the 3D manifold. This allows a portion of the coolant (50–80%) to bypass the microchannels in the cold plate to the exit plenum. As a result, the pressure was reduced by ∼66% compared to the conventional 3D manifold microchannel cooler.*
[DOI: 10.1115/1.4069319]

*Keywords: embedded cooling, 3D manifold microchannel, large-area cooling, CFD analysis*

## 1 Introduction

The power consumption of data centers in the U.S. is predicted to increase to 35 gigawatts (GW) by 2030, compared to 17 GW in 2022 [1]. This significant rise is attributed to the growing need for AI and machine learning-ready infrastructure, which requires more power and advanced cooling systems to manage the increased workload [2]. Moreover, recent advanced three-dimensional (3D)-chip packaging methods, such as chiplet heterogeneous integration techniques, have been developed to improve electronic performance while increasing the overall size of the microprocessor and packaging due to the limits of nanoscale-patterning [3]. For example, in the early 2000s, the size of a typical graphic processing unit (GPU) die was just 100 mm$^2$, however, it increased to a range of 600–800 mm$^2$ in 2020 while the thermal design power kept increasing up to 300 W

The International Technical Conference on Packaging and Integration of Electronic and Photonic Microsystems (InterPACK), Hotel FERA Anaheim, a DoubleTree by Hilton. InterPACK2024.
[1]Corresponding author.
Contributed by the Electronic and Photonic Packaging Division of ASME for publication in the Journal of Electronic Packaging. Manuscript received February 28, 2025; final manuscript received June 23, 2025; published online September 2, 2025. Assoc. Editor: Nakul Kothari.

 Copyright © 2025 by ASME 

[4]. Thus, as both the overall packaging size and processing power (heat generation) increase, more uniform cooling over larger microprocessors must be considered [5]. Conventional microchannel or micropin fins utilizing single-phase heat transfer possess the advantage of simplified design due to fewer geometric parameters requiring consideration. However, they are prone to performance degradation or mechanical bursting risks due to nonuniform temperature distributions along the flow direction and significantly high-pressure drops. As one of the solutions, manifold microchannels (MMCs) can be employed. The manifold structure integrated above the channels ensures a uniform distribution of fluid into each channel, thereby facilitating an even temperature distribution [6]. Furthermore, the significantly shortened flow path within the microchannels results in a reduced pressure drop compared to traditional microchannels, allowing for designs that are less sensitive to thermal-fluidic performance along the chip size.

Several studies regarding MMCs have shown that thermal uniformity is a key challenge for enhancing the cooling chip over the footprint area. Yang et al. [7] proposed a Z-type MMC heat sink architecture over $5 \times 5\,\text{mm}^2$ silicon footprint area using single-phase water flow. Their study effectively showcased the benefits of trapezoidal manifold designs over rectangular ones in improving fluid distribution uniformity and reducing thermal resistance. Zhou et al. [8] proposed a topologically optimized MMC for divertor thermal management using copper alloy. Their structural optimization focused on the microchannel substrate without fully addressing manifold flow distribution, showing low flowrate discrepancies ranging from −6% to +8%. Kim et al. [9] numerically performed a thermohydraulic analysis of MMC under full-scale simulation. Their design process primarily focused on adjusting geometrical parameters, such as manifold height and inlet-to-outlet width ratios without employing active manifold reshaping. As a result, significant flow maldistribution remained, yielding higher temperatures in the front-side cooled chips.

Although significant efforts have been made to mitigate thermal nonuniformity in MMC structures, they yet to sufficiently address large-area silicon-based coolers for achieving high cooling performance. Previous work by the authors [10–12], demonstrated a single-phase embedded silicon-based microchannels with a 3D manifold microcooler. Jung [10] demonstrated microcoolers with heat flux exceeding $q'' = 1\,\text{kW/cm}^2$ and a pressure drop of $\Delta P = 30\,\text{kPa}$ over a heated area of $A_h = 5 \times 5\,\text{mm}^2$. Wei et al. [11] conducted computational fluid dynamics (CFD) modeling of area-scaled silicon-based microcoolers [12] to a footprint of $24 \times 24\,\text{mm}^2$ and a manifold channel height of 700 $\mu$m, targeting thermal resistance of $R'' = 0.05\,\text{cm}^2\,^\circ\text{C/W}$. However, the results indicated a significant pressure drop of $\Delta P = 150\,\text{kPa}$ and pronounced temperature nonuniformity, which were primarily attributed to the nonuniform velocity distribution that persisted throughout the length of the inlet manifold. This behavior is likely a consequence of inertial effects and abrupt flow deceleration occurring near the downstream end of the channel.

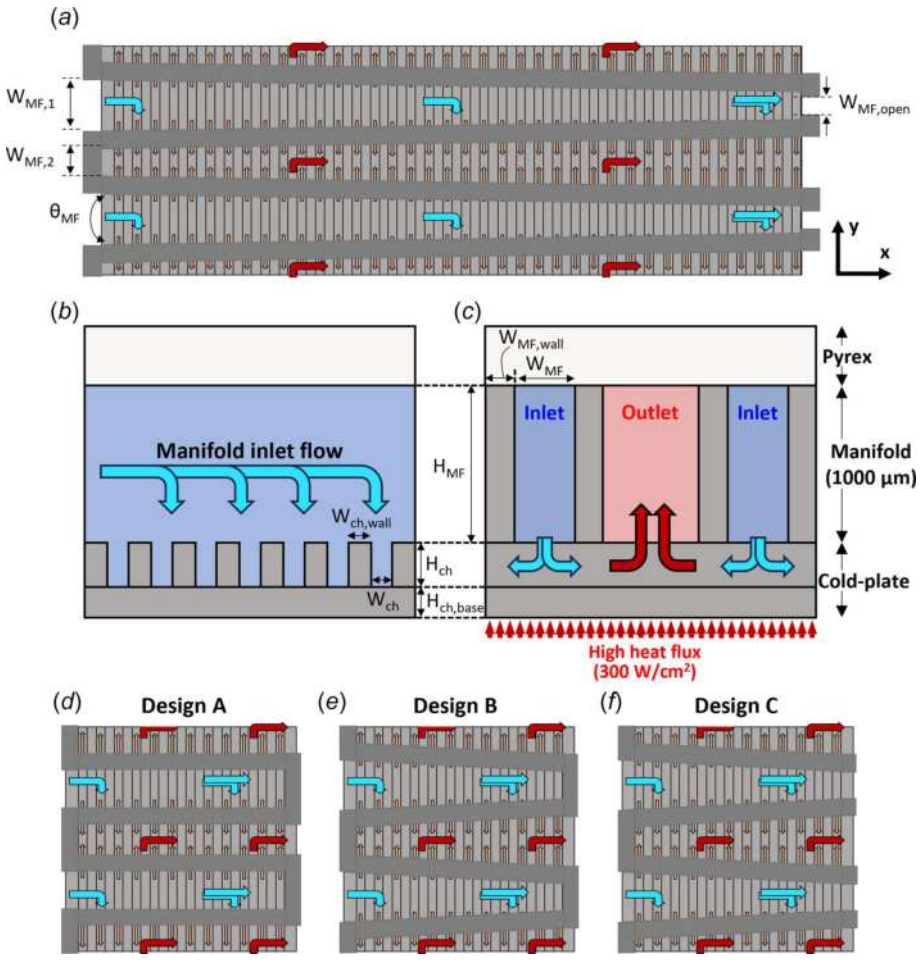


**Fig. 1** (*a*) A top-down view of the embedded manifold microchannel (not to scale), (*b*) a cross-sectional view along the *x*-axis at the manifold inlet conduit, and (*c*) a front view along the *y*-axis across the manifold conduits. (*d*)–(*f*) The representative manifold configurations, Design A (parallel manifold walls), B (converging–diverging conduits with closed ends), and C (converging–diverging conduits with closed end). The specific dimensions used in the parametric study on each MMC are detailed in Table 1.

In this work, we have carefully optimized a $30 \times 30\,\text{mm}^2$ silicon-based embedded microcooler with a 3D manifold structure (1 mm height) and cold plate microchannels using the commercial CFD package, ANSYS FLUENT, with a primary focus on improving flow and temperature uniformity, across the large-area footprint, while maintain low pressure drop. Starting from a baseline parallel manifold design, we introduced new manifold geometries and conducted extensive parametric optimization to minimize flow maldistribution. Furthermore, we analyzed the effect of inlet mass flowrate variations on the thermal resistance and pressure drop characteristics of the optimized MMC design.

## 2 Numerical Modeling

Figure 1 shows the design variables of the manifold and microchannel cold plate where the microchannel width is equal to the channel wall width, i.e., $W_{ch} = W_{ch,wall}$; and base thickness ($H_{ch,base}$) is set at 100 $\mu$m. The height of the manifold ($H_{MF}$) and wall thickness ($W_{MF,wall}$) are 1 mm and 150 $\mu$m, respectively.

Design A represents the baseline microcooler configuration with parallel manifold channels.

In Design B, we consider the impact of converging–diverging manifold conduits, tilting angles: $\theta_{MF} = 0.19$ deg, 0.57 deg, 0.95 deg, and 1.15 deg, to achieve a more uniform flow and temperature distributions over the footprint of the large area microcooler.

To further reduce the excessive pressure drop, a novel approach was implemented in Design C by introducing an opening at the downstream end of the inlet manifold conduit. This modification enabled a portion of the coolant to bypass directly to the outlet plenum, thereby substantially alleviating the pressure build-up due to decelerating flow. The detailed geometric specifications of each MMC design are summarized in Table 1.

We conducted CFD modeling on a representative unit cell ($0.5 \times 30\,\text{mm}^2$) of a full-scale ($30 \times 30\,\text{mm}^2$) microcooler, shown in Fig. 2 to effectively capture the relevant flow physics while significantly reducing computational cost. The mass flowrate at the inlet was specified within the laminar flow regime, ranging from 25 to 100 g/min corresponding to a Reynolds number of $\text{Re}_{ch} = 28$–$110$ within the microchannel cold plate and $\text{Re}_{MF,in} = 500$–$2470$ at the inlet manifold. The inlet temperature is set at 60 °C and a gauge pressure of 0 Pa was imposed at the outlet boundary. To prevent backflow, both the inlet and outlet conduits were extended by an additional 1 mm. A constant heat flux of $q'' = 300\,\text{W/cm}^2$ was applied to the bottom surface of the cold plate for a moderate heat flux. Given the extended flow path length of 30 mm, ensuring sufficient mass flow through the cold plate and achieving temperature uniformity were critical to optimizing both thermal and hydraulic performances. Therefore, the MMC domain was segmented into 20 sections at 1.5 mm intervals to track the local heater temperatures and assess coolant flow distribution.

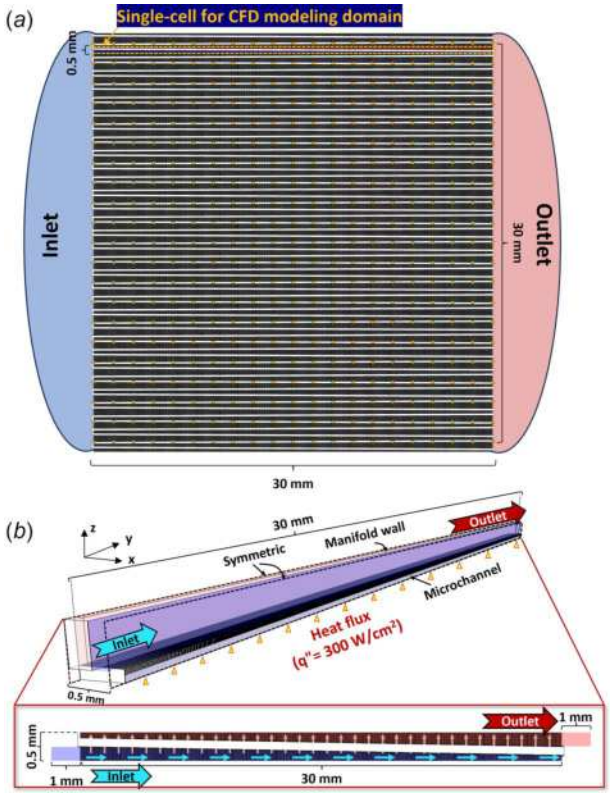


**Fig. 2 (*a*) Schematic of the full-scale large-area microcooler with a cooling area of $30 \times 30\,\text{mm}^2$ and (*b*) unit cell model used for the CFD domain over $0.5 \times 30\,\text{mm}^2$, the side walls were set to the symmetric boundary condition**

To ensure accurate resolution of boundary layer phenomena, flow structures, and overall conjugate heat transfer behavior, a polyhedral mesh with inflation layers was employed in both the fluid and solid domains. The inflation layers were used to precisely capture near-wall gradients and boundary layer thickness, as illustrated in Appendix A. A mesh independence study was performed across a range of 15–33 million cells, accounting for the smallest geometric features within the microchannel. Based on a balance between computational cost and solution accuracy, an optimal mesh size of approximately 27 million cells was selected. Detailed results of the mesh independence test are provided in Appendix A.

The simulations were conducted using the pressure-based coupled solver in ANSYS FLUENT, assuming steady-state, incompressible, and single-phase flow conditions based on the modeling discussion. The governing equations solved included the continuity,

**Table 1 Parametric set for the various MMC designs (unit: $\mu$m)**

| | Manifold | | | | $\mu$-channel | | | |
|---|---|---|---|---|---|---|---|---|
| Design | $W_{MF}$ ($W_{MF,1}/W_{MF,2}$) | $W_{MF,wall}$ | $H_{MF}$ | $W_{MF,open}$ | $W_{ch}$ | $W_{ch,wall}$ | $H_{ch}$ | $H_{ch,base}$ |
| A1 | 350 | 150 | 1000 | — | 15 | 15 | 125 | 100 |
| A2 | 350 | 150 | 1000 | — | 15 | 15 | 100 | 100 |
| A3 | 350 | 150 | 1000 | — | 15 | 15 | 75 | 100 |
| A4 | 350 | 150 | 1000 | — | 15 | 15 | 50 | 100 |
| B1 | 400/300 ($\theta_{MF} = 0.19$ deg) | 150 | 1000 | — | 15 | 15 | 125 | 100 |
| B2 | 500/200 ($\theta_{MF} = 0.57$ deg) | 150 | 1000 | — | 15 | 15 | 125 | 100 |
| B3 | 600/100 ($\theta_{MF} = 0.95$ deg) | 150 | 1000 | — | 15 | 15 | 125 | 100 |
| B4 | 650/50 ($\theta_{MF} = 1.15$ deg) | 150 | 1000 | — | 15 | 15 | 125 | 100 |
| C1 | 500/200 | 150 | 1000 | 200 | 15 | 15 | 125 | 100 |

Design A features variations in cold plate channel height, while Designs B and C focus on the modifications to the manifold angle and bypassing opening.

momentum, and energy equations for both the fluid and solid domains:

Continuity (fluid domain)

$$\frac{\partial}{\partial x_i}(\rho u_i) = 0 \tag{1}$$

Momentum (fluid domain)

$$\frac{\partial}{\partial x_i}(\rho u_i u_j) = -\frac{\partial P}{\partial x_i} + \frac{\partial}{\partial x_i}\left(\mu \frac{\partial u_j}{\partial x_i}\right) \tag{2}$$

Energy (fluid domain)

$$\frac{\partial}{\partial x_i}(\rho u_i C_p T_{\text{liq}}) = \frac{\partial}{\partial x_i}\left(k_{\text{liq}} \frac{\partial T_{\text{liq}}}{\partial x_i}\right) \tag{3}$$

Energy (solid domain)

$$\frac{\partial}{\partial x_i}\left(k_{\text{sol}} \frac{\partial T_{\text{sol}}}{\partial x_i}\right) = 0 \tag{4}$$

## 3 Data Reduction

The thermal performance of the microcooler was assessed based on two key metrics: thermal resistance and pumping power, representing the heat transfer and hydraulic characteristics, respectively. The overall thermal resistance, $R''_{\text{tot}}$, is determined by using a thermal resistance network as

$$R''_{\text{tot}} = \frac{\bar{T}_h - T_{f,\text{in}}}{q''} \tag{5}$$

where $\bar{T}_h$ is the mean temperature of heater aera and $T_{f,\text{in}}$ is the inlet fluid temperature which is 60 °C in this study. $q''$ indicates the applied heat flux, which is a constant as 300 W/cm$^2$.

The conduction thermal resistance $R''_{\text{cond}}$ determined from the silicon substrate is expressed as

$$R''_{\text{cond}} = \frac{\bar{T}_h - \bar{T}_b}{q''} = \frac{H_{\text{ch,base}}}{k_{\text{si}}} \tag{6}$$

where $\bar{T}_b$ is the temperature of the microchannel base area. Conduction thermal resistance also can be simply defined from silicon base height ($H_{\text{ch,base}}$) and the thermal conductivity of silicon ($k_{\text{si}}$). For silicon thermal conductivity, we have used the temperature-dependent thermal conductivity as following the previous literature [13].

Advection resistance $R''_{\text{adv}}$ determined by the increase of fluid temperature is calculated as

$$R''_{\text{adv}} = \frac{T_{f,\text{avg}} - T_{f,\text{in}}}{q''} \tag{7}$$

where $T_{f,\text{avg}}$ is the mean fluid temperature between inlet and outlet.

Convection thermal resistance $R''_{\text{conv}}$ is expressed as

$$R''_{\text{conv}} = \frac{1}{h_{\text{eff}}} = R''_{\text{tot}} - R''_{\text{cond}} - R''_{\text{adv}} \tag{8}$$

where $h_{\text{eff}}$ is the effective heat transfer coefficient based on the average channel temperature of cooler.

To quantify the degree of temperature nonuniformity, a thermal uniformity index (TUI) is introduced, defined as the ratio of thermal resistances as

$$\text{TUI} = \frac{R''_{\text{tot,avg}}}{R''_{\text{tot,max}}} \tag{9}$$

The pumping power, representing the energy required to drive the liquid coolant through the microcooler, is defined as

$$P_{\text{pump}} = \frac{\dot{m}}{\rho}\Delta P \tag{10}$$

where $\dot{m}$ is the mass flowrate and $\Delta P$ is the pressure drop.

## 4 Results and Discussion

Parametric studies were conducted on each variable of the MMC design, including microchannel height, manifold angle, and manifold opening. Prior to analyzing the cooler's performance, we validated the CFD-predicted pressure drop against experimental results. This validation employed the as-fabricated silicon-based microcoolers, each with a 30 mm × 30 mm footprint. Detailed comparison results are provided in Appendix B. A separate paper describing the experimental setup and datasets is currently under preparation. In this study, we mainly focus on discussing the primary findings that impact the hydraulic–thermal uniformity and performance. First, varying the microchannel width, $W_{\text{ch}}$, did not result in significant performance differences, as the cross-sectional microchannel area remained the same due to the constant channel porosity of 0.5, leading to unchanged velocity distribution with increased channel width detailed in Appendix C. Specifically, we observed a substantial difference between the average and maximum junction temperatures in Design A1 basically due to the nonuniformity in the mass flowrate from the inlet to the outlet cold plate microchannels, see Fig. 3. This is caused by a remaining flow momentum at the end

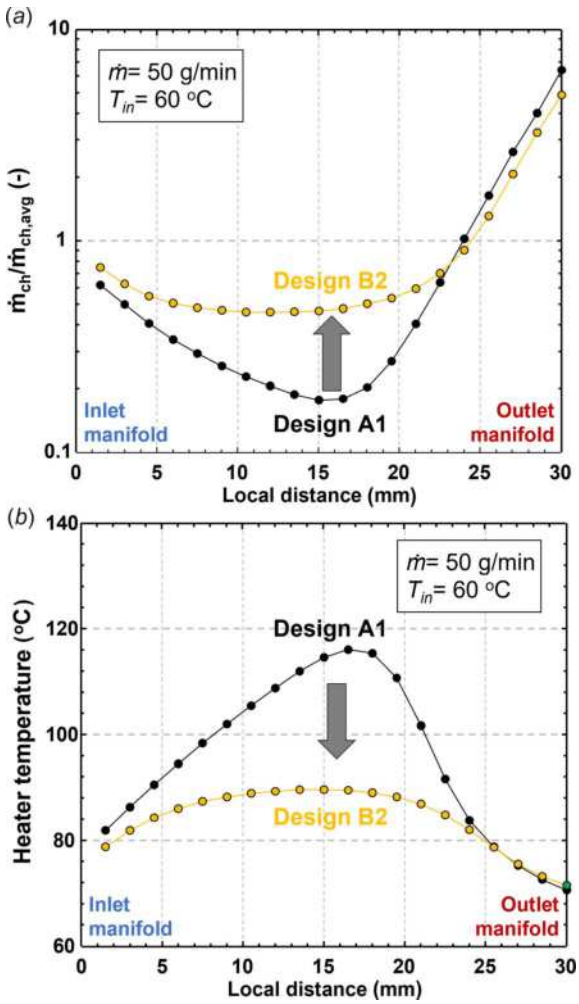


**Fig. 3 Comparison of the effect of parallel (Design A1) and converging–diverging 3D manifold walls (Design B2) on (*a*) mass flowrate distributions and (*b*) temperature uniformity over the microcooler footprint**

**Table 2 Hydraulic–thermal performances of the featured MMC unit-cell designs at the inlet mass flowrate of 50 g/min and heat flux of 300 W/cm$^2$**

| Design index | $\bar{T}_h$ (°C) | $T_{h,\max}$ (°C) | $R''_{\text{tot,avg}}$ (cm$^2$ °C/W) | $R''_{\text{tot,max}}$ (cm$^2$ °C/W) | TUI | $\Delta P$ (kPa) | $P_{\text{pump}}$ (mW) |
|---|---|---|---|---|---|---|---|
| A1 | 94.4 | 116 | 0.12 | 0.188 | 0.63 | 38.7 | 32.9 |
| B2 | 82.6 | 89 | 0.08 | 0.097 | 0.82 | 24.5 | 20.8 |
| C1 | 86.2 | 90.7 | 0.087 | 0.102 | 0.90 | 13.0 | 12.1 |

region of the inlet manifold conduit. As summarized in Table 2, the TUI exhibited a 0.63, indicating a ∼66% higher maximum temperature compared to the average heater temperature. However, when the channel height was reduced from 125 $\mu$m to 50 $\mu$m from Design A1 to A4, both thermal performance and thermal uniformity slightly improved compared to the baseline Design A1. These improvements stem from the higher flow velocity and elevated convective heat transfer coefficient associated with the reduced channel cross-sectional area. However, this thermal enhancement was accompanied by a slight rise in pressure drop, from 38.7 kPa for A1 to 40.1 kPa for A4.

Given the inherent limitations of addressing flow nonuniformity exclusively through microchannel design modifications, we shifted our focus to innovating the three-dimensional manifold. In the baseline, Design A1, the manifold channels are constituted with parallel walls (uniform cross-sectional area along the flow direction). Since the main reason for the flow nonuniformity is due to the inertial momentum at the end of the manifold inlet. We considered variable cross section (inlet manifold walls tilt angle of $\theta_{\text{MF}} = 0.34$ deg, Design B2). By narrowing (converging) the inlet and widening (diverging) the outlet, the design reduces abrupt pressure changes and distributes the flow more evenly across the channel array. The comparisons of flow and temperature distribution are depicted in Fig. 3(*a*). The average channel mass-flowrate, $\dot{m}_{\text{ch,avg}}$, is defined as the total inlet mass flow divided by the number of discrete segments ($N = 20$ in this study), whereas $\dot{m}_{\text{ch}}$ denotes the local channel mass-flowrate extracted from the CFD simulations. In an ideal manifold configuration, the ratio $\dot{m}_{\text{ch}}/\dot{m}_{\text{ch,avg}}$ remains 1 for all segments, thereby ensuring perfectly uniform flow distribution. Transitioning from the conventional parallel MMC to a converging–diverging MMC markedly improved flow uniformity: regions previously exhibiting flow deficits in the parallel manifold approached $\dot{m}_{\text{ch}}/\dot{m}_{\text{ch,avg}} = 1$. As a result, the peak temperature nonuniformity was reduced from $\Delta T_{\max} = 46$ K in the conventional MMC to $\Delta T_{\max} = 18$ K in the converging–diverging MMC, yielding TUI of 0.82, as illustrated in Fig. 3(*b*). We further investigated the influence of the manifold-wall angle in our converging–diverging manifold. Subject to geometric constraints, the manifold angle was varied from $\theta_{\text{MF}} = 0.19$ deg in Design B1 to 1.15 deg in Design B4. Figure 4(*a*) shows the local heater temperature profiles for each configuration. Compared to Design A1, increasing the manifold angle suppressed the midspan peak temperature. However, when the angle was increased from B2 to B4, the steeper walls enlarged the inlet-channel cross section and caused flow deficiency near the inlet region. TUI analysis, therefore, identifies an optimal manifold angle that best balances temperature uniformity as shown in Fig. 4(*b*). Nevertheless, a residual flow accumulation persisted near the end of the inlet manifold conduit. To mitigate this, Design C incorporates an aperture at the downstream end of the inlet manifold conduit, which relieves excess flow and further smooths the mass-flow distribution—thereby enhancing thermal uniformity while simultaneously reducing pressure drop.

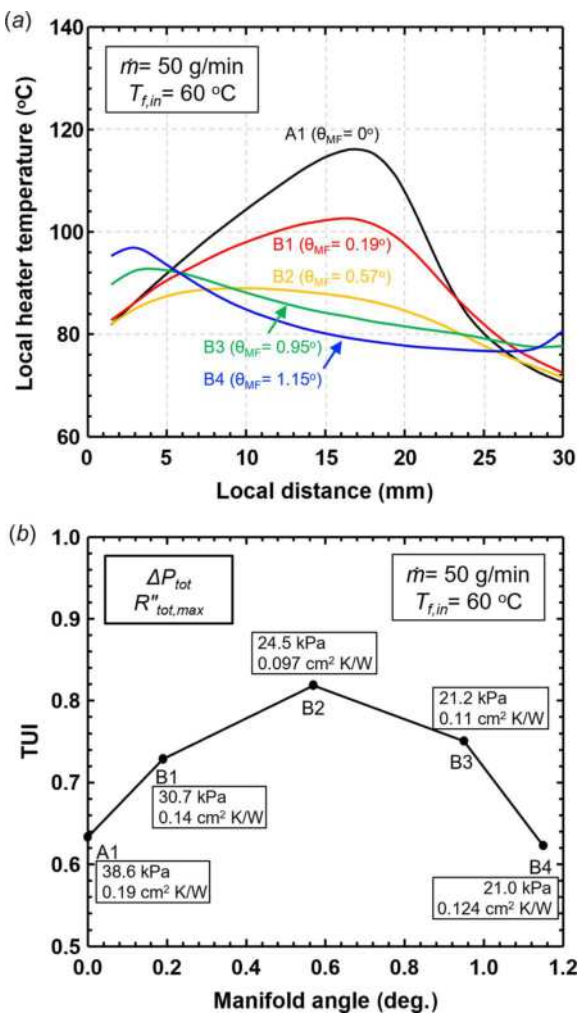


**Fig. 4 (*a*) Effect of manifold wall angle on temperature nonuniformity along the 30 mm flow direction and (*b*) identification of the optimal manifold wall angle based on the TUI analysis**

Figure 5 presents the local pressure distributions along the centerline of the inlet manifold conduit (A–A′), across the midsection of the microchannel (B–B′), and along the centerline of the outlet manifold conduit (C–C′) for Design C1 with the incorporated opening. In each region, the pressure profile follows an almost linear decline, indicating a uniform pressure gradient throughout the heating area. This homogeneous pressure drop fosters a consistent flowrate by minimizing disturbances along the flow path, which in turn promotes improved temperature uniformity. Figure 6(*a*) directly demonstrates the local temperature variation between our optimizing MMC (Design C1) having both converging–diverging manifold and manifold opening and the conventional MMC that has been studied by Wei et al. [11]. The comparable dimensions for each microcooler are listed in Table 3. The parallel manifold that they introduced showed unsatisfactory thermal uniformity over the entire heated surface. Similar to the results of our previous parametric study in Design A, they observed a hotspot located in the mid-to-late flow region, with the temperature difference between the minimum and maximum temperatures reaching as high as $\Delta T_{\max} = 36$ K.

On the contrary, under the same operating conditions, improved MMC design demonstrated exceptional thermal uniformity with a maximum temperature difference of $\Delta T_{\max} = 4$ K, despite a slight reduction in effective flowrate due to the opening at the end of the inlet manifold conduit. Moreover, average thermal resistance as a

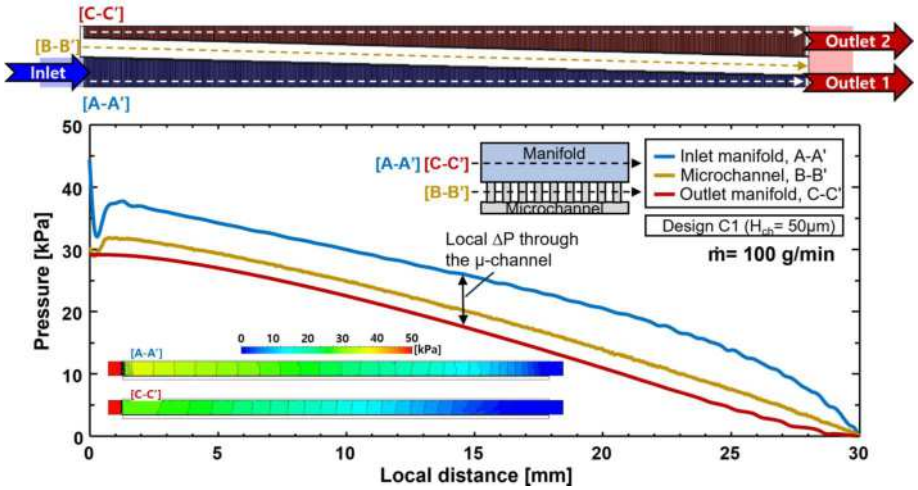


**Fig. 5 Local pressure along the converging–diverging manifold inlet channel (A-A'), underneath the manifold wall (B-B'), and manifold outlet channel (C-C') in the presence of the opening at the end of the manifold inlet channel**

function of pressure drop was compared at different flow rates as depicted in Fig. 6(*b*). Wei et al. [11] proposed that increasing the height of the manifold conduit from 700 $\mu$m to 1500 $\mu$m decreased the manifold pressure drop, thereby improving flow uniformity within the microchannels by alleviating inertial momentum. However, due to the limitations of microchip packaging, adjusting the lateral dimensions of the manifold conduit could be a more effective approach to achieving better flow and thermal uniformity. Our converging–diverging MMC design achieved much smaller thermal resistance by improving flow and therefore temperature uniformity across the heating area while reducing the pressure drop. At a maximum flowrate of $\dot{m} = 100$ g/min, the pressure drop and thermal resistance were reduced by 50% and 38%, respectively, compared to the conventional MMC with a height of 1500 $\mu$m. This resulted in a total thermal resistance of $R'' = 0.055$ cm$^2$ K/W, while maintaining the pressure drop under $\Delta P = 42$ kPa.

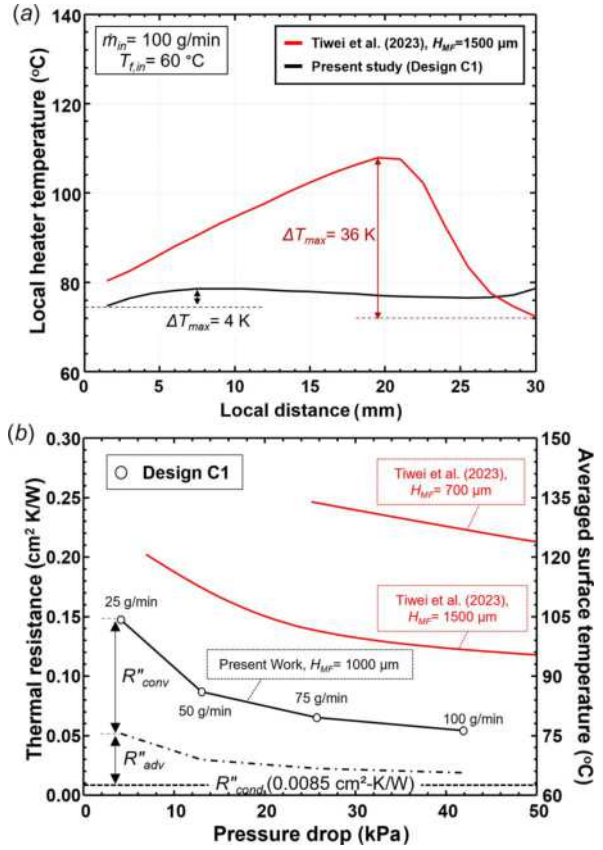


**Fig. 6 (*a*) Comparison of local heater temperature distribution at the mass flowrate of 100 g/min. For the performance comparison, the previous MMC geometries were adopted [11]. (*b*) Average total thermal resistance as a function of pressure drop of large-area microcooler.**

Figure 7(*a*) shows the variation in local temperature distribution on the featured MMCs. To address thermal nonuniformity in the large-area embedded microcooler, we attempted to modify the geometries of the manifold and cold plate. The factor that has the greatest influence on uniformity was the manifold shape rather than the microchannel, and it was confirmed that once the shape was changed from the parallel to a converging–diverging shape, the flow imbalance could be greatly resolved ($\Delta T_{\max,B2} = 17$ K, TUI = 0.82). Moreover, the introduction of the slit led to an inverse increase in the temperature and further enhanced the thermal uniformity at the end of the manifold inlet conduit by intentionally bypassing the liquid ($\Delta T_{\max,C1} = 8$ K, TUI = 0.9). Figure 7(*b*) summarizes the maximum total thermal resistance as a function of pressure drop in the designed MMC at a constant mass flowrate of $\dot{m} = 50$ g/min. This result shows how the thermal resistance and pressure drop are reduced by changing the geometric dimensions. Variations to the microchannels in Designs A1 to A4 showed that as the hydraulic diameter decreased, thermal resistance also decreased, while the pressure drop slightly increased due to higher flow velocity and improved boundary layer disruption. Designs B and C, which alter the manifold geometry to enhance flow uniformity, delivered substantial enhancements in hydraulic–thermal performance. In particular, the optimized large-area microcooler (Design C1) reduced pressure drop by approximately 66% and maximum thermal resistance by about 45% relative to Design A1. This lower pressure drop also decreases the pumping power required to circulate the coolant. Further details on the analysis of pumping power are provided in Appendix D. However, when the microchannel height was reduced to $H_{ch} = 50$ $\mu$m, channel pressures was as high as the manifold pressure, and using Design C again elevated the peak temperature because of the increased liquid loss at the slit opening and breaking the flow uniformity, resulting in higher maximum thermal resistance. Thus, the comprehensive thermal–hydraulic performance as the flowrate increased is shown in Fig. 7(*c*). In MMCs with relatively small hydraulic diameters ($H_{ch} = 50$ $\mu$m)—where high internal channel pressures have already been resolved by the converging–diverging manifold—thermal nonuniformity reappears

Table 3 Dimensions of the previous and optimized MMC (unit: $\mu$m)

| Case | Manifold | | | | $\mu$-channel | | | |
|---|---|---|---|---|---|---|---|---|
| | $W_{MF}$ ($W_{MF,1}/W_{MF,2}$) | $W_{MF,wall}$ | $H_{MF}$ | $W_{MF,open}$ | $W_{ch}$ | $W_{ch,wall}$ | $H_{ch}$ | $H_{ch,base}$ |
| Design C1 | 500/200 | 150 | 1000 | 200 | 15 | 15 | 125 | 100 |
| Reference [11] | 250/250 | 200 | 700 | — | 90 | 90 | 300 | 100 |

even when an opening was implemented. In contrast, for those configurations exhibiting persistent temperature nonuniformity ($H_{ch} = 125$ $\mu$m), adding an outlet slit at the end of the inlet conduits effectively mitigates these profile deviations. This finding illustrates that microcooler performance can be enhanced not only by enlarging the channel cross section but also by actively promoting in-channel temperature uniformity.

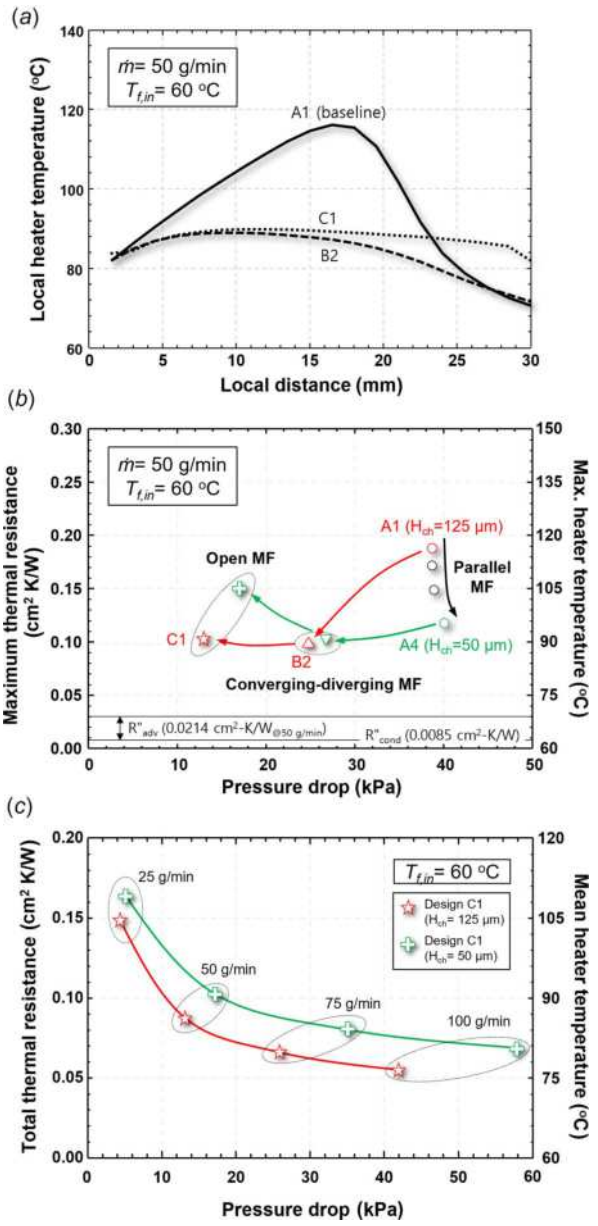


**Fig. 7 (*a*) Comparison of thermal uniformity among the featured MMC configurations, (*b*) optimizing process of the maximum thermal resistance and pressure drop by alleviating the pressure drop and thermal resistance, and (*c*) thermal–hydraulic performance comparison for different microchannel heights under the Design C1 manifold configuration**

## 5 Conclusion

In this work, a $30 \times 30\,mm^2$ silicon microcooler with a 3D manifold and cold plate microchannels were optimized using ANSYS FLUENT to enhance thermal and hydraulic performance. Various design configurations (A to C) were analyzed, focusing on microchannel width, height, manifold angles, and openings to address nonuniform temperature distribution and pressure drops. The most significant improvements were observed in designs incorporating a converging–diverging manifold with an opening, which reduced pressure drop and enhanced thermal uniformity. Specifically, Design C demonstrated a substantial reduction in pressure drop (66.3%) and thermal resistance (45.6%), achieving a thermal resistance of 0.055 $cm^2$ K/W and maintaining a pressure drop under 42 kPa at a maximum flowrate of 100 g/min.

Future work remains focusing on expanding this study to account for variable heat flux conditions, thinner cold-plate base substrate, and potential surface coating enhancements. Additionally, comparative analysis using alternative coolant fluids and long-term reliability evaluations, including clogging effects and flow profile degradation in the experiment, will be pursued to further validate the robustness of the proposed cooling strategies.


## Funding Data

- The National Science Foundation Engineering Research Center for Power Optimization of Electro Thermal Systems (POETS) (Sub-Award No. 073708-14989/Award No. EEC-1449548; Funder ID: 10.13039/100000001).


## Data Availability Statement

The datasets generated and supporting the findings of this article are obtainable from the corresponding author upon reasonable request.

## Nomenclature

$A_h$ = heating area, $cm^2$
$C_p$ = specific heat, J/kg K
$H_{ch}$ = height of microchannel, $\mu$m
$H_{ch,base}$ = base thickness of cold-plate, $\mu$m
$H_{MF}$ = height of manifold conduit, $\mu$m
$k$ = thermal conductivity, W/m K
$\dot{m}$ = mass flow rate, g $min^{-1}$
$\dot{m}_{ch}$ = mass flow rate per channel, g/min
$P_{pump}$ = pumping power, W
$q''$ = heat flux, W/$cm^2$
$R''_{tot,ave}$ = total thermal resistance based on the average temperature, $cm^2$ K/W
$R''_{tot,max}$ = total thermal resistance based on the maximum temperature, $cm^2$ K/W
Re = Reynolds number
$T_{h,ave}$ = average heater temperature, °C
$T_{h,max}$ = maximum heater temperature, °C
$u$ = velocity, m/s
$W_{ch}$ = width of microchannel, $\mu$m

$W_{ch,gap}$ = width of microchannel gap, $\mu$m
$W_{ch,wall}$ = thickness of microchannel wall, $\mu$m
$W_{MF}$ = width of manifold conduit, $\mu$m
$W_{MF,open}$ = width of manifold opening, $\mu$m
$W_{MF,wall}$ = thickness of manifold wall, $\mu$m
$\Delta P$ = pressure drop, kPa
$\Delta T_{h,max}$ = maximum temperature difference, °C
$\theta_{MF}$ = angle of converging–diverging manifold, deg
$\rho$ = density, kg/m$^3$
TUI = thermal uniformity index

## Appendix A: Mesh Independence Test

As shown in Fig. 8(*a*), a mesh test was conducted using a range of 15–33 million meshes, considering the smallest feature size in the microchannel. The boundary conditions were set with a mass flowrate of 50 g/min, an inlet temperature of 60 °C, and a heat flux of 300 W/cm$^2$. As shown in Fig. 8(*b*), all selected meshing methodologies provided highly accurate predictions for both thermal performance (maximum difference observed with mesh refinement = 0.28%) and pressure drop (maximum difference observed with mesh refinement = 1.37%). Considering the computational cost and solution reliability, we selected an optimal mesh size of approximately 27 million meshes within the tested range.

## Appendix B: Comparison of Computational Fluid Dynamics Results With Experiment

Figure 9 presents a comparison of pressure drop between CFD simulations and experimental measurements for the Design B configuration. The comparison was conducted under adiabatic conditions across a flowrate range of 0.5–2 L/min. The mean absolute error over this range was approximately 10%, indicating good agreement between the simulation and experimental results, despite potential geometrical uncertainties introduced during sample fabrication. As this study primarily focuses on thermo–hydraulic analysis using CFD, detailed descriptions of the experimental procedures as well as the corresponding thermal performance results are reported in a separate article.

## Appendix C: Effect of Channel Width on Thermal Uniformity

Figure 10(*a*) displays the ratio of local mass flowrate within the microchannel. The significant inertial flow in the manifold inlet channel resulted in a high flow concentration near the end of the channel (within the distance range of 24–30 mm), accounting for almost 70% of the total mass flowrate. Thus, the remaining 80% of the heating surface area did not adequately dissipate the heat, leading to significant thermal nonuniformity as illustrated in

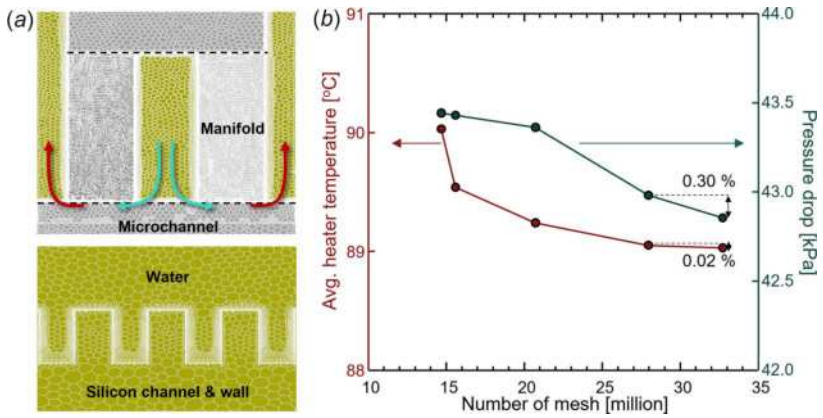


**Fig. 8 (*a*) Polyhedral meshes in the fluid and solid domains and (*b*) the results of mesh dependency on unit cell simulation**

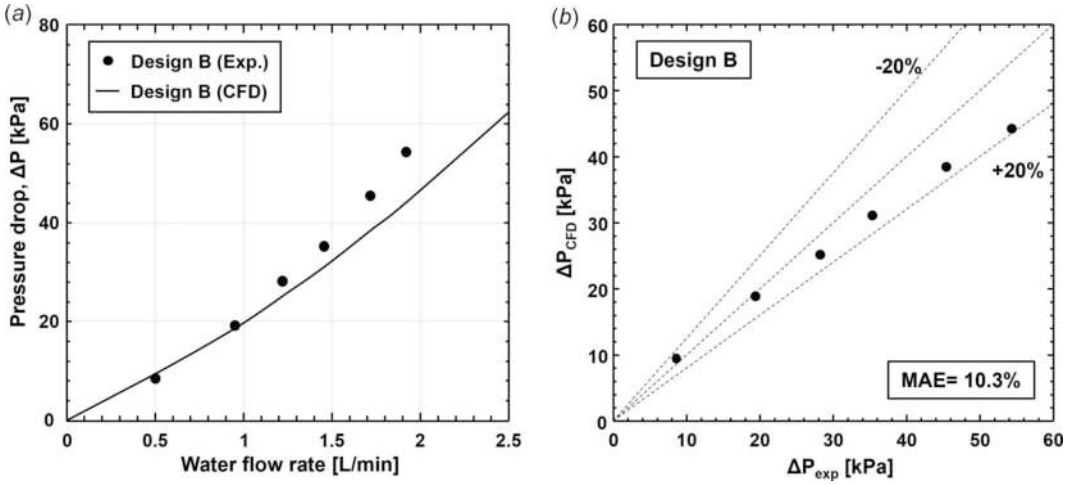


**Fig. 9 Pressure drop validation with experimental data**

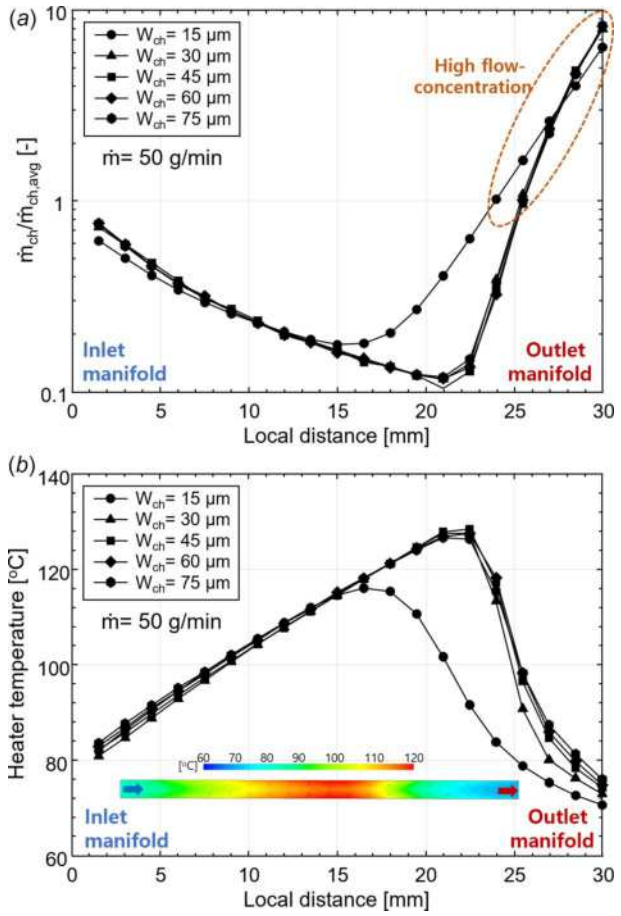


**Fig. 10 Distribution of (*a*) local mass flowrate flowing in the channel of the cold plate and (*b*) local heated temperature of the heater surface with respect to the channel width of the cold plate**

Fig. 10(*b*). The temperature difference over the heating surface ranged from $\Delta T_{max} = 46–55$ K, depending on the width of the microchannel. As with the effect of channel width of the cold plate, the effect of microchannel height also showed similar nonuniform flow and temperature trends in Design A.

## Appendix D: Analysis of Pumping Power

Based on unit-cell simulation results for a $0.5 \times 30\,mm^2$ heated area, we expanded the analysis to cover a total cooling area of $30 \times 30\,mm^2$ to assess the actual pumping power. In our study, as parametric analysis was conducted under a constant mass flowrate, the pumping power was proportional to the pressure drop, as illustrated in Fig. 11. Compared to the baseline A1 design, transitioning to manifold structures (Designs B and C) significantly reduced the pumping power, resulting in a 36.6–66.4% improvement in energy consumption. Notably, incorporating an opening at

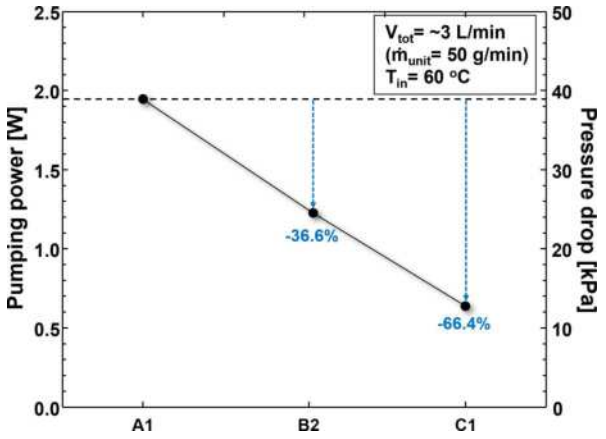


**Fig. 11 Comparison of the pumping power on the representative MMC design on the footprint area of $30 \times 30\,mm^2$**

the end of the manifold inlet conduit, from Design B2 to Design C1, reduced the pumping power from 1.3 W to 0.66 W, demonstrating a 47% improvement in power consumption.

## References


[1] International Energy Agency, 2024, "Electricity 2024, Analysis and Forecast to 2026," IEA, Paris, France, https://www.iea.org/reports/electricity-2024

[2] ARPA-E, 2023, "Cooling Operations Optimized for Leaps in Energy, Reliability, and Carbon Hyperefficiency for Information Processing Systems," ARPA-E, Washington, DC.

[3] Lau, J. H., 2022, "Recent Advances and Trends in Advanced Packaging," IEEE Trans. Compon., Packag. Manuf. Technol., **12**(2), pp. 228–252.

[4] Sun, Y., Agostini, N. B., Dong, S., and Kaeli, D., 2020, "Summarizing CPU and GPU Design Trends With Product Data," e-print arXiv:1911.11313.

[5] Steller, W., Windrich, F., Bremner, D., Robertson, S., Mrosko, R., Keller, J., Brunschwiler, T., et al., 2018, "Microfluidic Interposer for High Performance Fluidic Chip Cooling," Proceedings of the 2018 7th Electronic System-Integration Technology Conference (ESTC), Dresden, Germany, Sept. 18–21, pp. 1–8.

[6] Boteler, L., Jankowski, N., McCluskey, P., and Morgan, B., 2012, "Numerical Investigation and Sensitivity Analysis of Manifold Microchannel Coolers," Int. J. Heat Mass Transfer, **55**(25–26), pp. 7698–7708.

[7] Yang, S., Li, J., Cao, B., Wu, Z., and Sheng, K., 2024, "Investigation of Z-Type Manifold Microchannel Cooling for Ultra-High Heat Flux Dissipation in Power Electronic Devices," Int. J. Heat Mass Transfer, **218**, p. 124792.

[8] Zhou, J., Lu, M., Han, L., Zhao, Q., Li, Q., and Chen, X., 2025, "Topological Manifold Microchannel Cooling for Thermal Management of Divertor in Fusion Reactor," Energy, **315**, p. 134145.

[9] Kim, Y., Kong, D., Selvakumar, R. D., Kang, M., Kang, N., Kwon, J., and Lee, H., 2025, "Thermal-Hydraulic Characterization in Manifold-Microchannel Heat Sinks for Energy-Efficient Cooling of HEV/EV Power Modules," Appl. Therm. Eng., **265**, p. 125611.

[10] Jung, K. W., 2020, "Investigating Thermo-Fluidic Performance of Si-Based Embedded Microchannels-3D Manifold Cooling System for High Power Density Electronic Applications," Ph.D. dissertation, Stanford University, Stanford, CA.

[11] Wei, T., Hazra, S., Lin, Y., Gupta, M. P., Degner, M., Asheghi, M., and Goodson, K. E., 2023, "Numerical Study of Large Footprint ($24 \times 24\,mm^2$) Silicon-Based Embedded Microchannel Three-Dimensional Manifold Coolers," ASME J. Electron. Packag., **145**(2), p. 021008.

[12] Jung, K. W., Kharangate, C. R., Lee, H., Palko, J., Zhou, F., Asheghi, M., Dede, E. M., and Goodson, K. E., 2019, "Embedded Cooling With 3D Manifold for Vehicle Power Electronics Application: Single-Phase Thermal-Fluid Performance," Int. J. Heat Mass Transfer, **130**, pp. 1108–1119.

[13] Shanks, H. R., Maycock, P. D., Sidles, P. H., and Danielson, G. C., 1963, "Thermal Conductivity of Silicon From 300 to 1400 K," Phys. Rev., **130**(5), pp. 1743–1748.